Phase separation and charge carrier self-organization in semiconductor-multiferroic $Eu_{0.8}Ce_{0.2}Mn_2O_5$

V. A. Sanina,[1,*] E. I. Golovenchits,[1] V. G. Zalesskii,[1] S. G. Lushnikov,[1] M. P. Scheglov,[1] S. N. Gvasaliya,[2] A. Savvinov,[3] R. S. Katiyar,[3] H. Kawaji,[4] and T. Atake[4]

[1]*A.F. Ioffe Physical Technical Institute, 26 Politekhnicheskaya, 194021 St. Petersburg, Russia*

[2]*Laboratory for Neutron Scattering, ETHZ & Paul Scherrer Institut, CH-5232 Villigen PSI, Switzerland*

[3]*University of Puerto Rico, San Juan, Puerto Rico*

[4]*Tokyo Institute of Technology, 4259 Nagatsuta-cho, Midori-ku, Yokohama 226-8503, Japan*

(Received 28 January 2008; revised manuscript received 8 October 2009; published 1 December 2009)

The state with a giant permittivity ($\varepsilon' \sim 10^4$) and ferromagnetism have been observed above 185 K (including room temperature) in single crystals of diluted semiconductor manganite-multiferroic $Eu_{0.8}Ce_{0.2}Mn_2O_5$ in the investigations of x-ray diffraction, heat capacity, dielectric and magnetic properties, conductivity, and Raman light-scattering spectra of this material. X-ray diffraction study has revealed a layered superstructure along the *c* axis at room temperature. A model of the state with a giant ε' including as-grown two-dimensional layers with doping impurities, charge carriers, and double-exchange-coupled Mn^{3+}-Mn^{4+} ion pairs is suggested. At low temperatures these layers form isolated electrically neutral small-size one-dimensional superlattices, in which de Haas–van Alphen oscillations were observed. As temperature grows and hopping conductivity increases, the charge carrier self-organization in the crystal causes formation of a layered superstructure consisting of charged layers (with an excess Mn^{3+} concentration) alternating with dielectric layers of the initial crystal—the ferroelectricity due to charge-ordering state. Ferromagnetism results from double exchange between Mn^{3+} and Mn^{4+} ions by means of charge carriers in the charged layers. Temperature evolution of frequency shifts of A_g modes and quasielastic scattering in Raman-scattering spectra agree with the pattern of phase transitions in ECMO suggested.

DOI: 10.1103/PhysRevB.80.224401 PACS number(s): 75.47.Lx, 76.50.+g, 77.80.−e

I. INTRODUCTION

Orthorhombic crystals of manganites RMn_2O_5 (*R* rare-earth ions: Y and Bi) are multiferroics in which long-range magnetic and ferroelectric orders are realized at $T < 30-40$ K. A strong coupling between magnetic and ferroelectric states resulting from nearly equal temperatures of magnetic and ferroelectric orderings attracts a considerable attention of researchers to these materials (see Refs. 1–4 and references therein). The multiferroics with similar ordering temperatures offer a unique possibility to manipulate the magnetic and polar states by applying electric and magnetic fields, respectively, which makes them attractive candidates for different applications, especially when coupled magnetic and polar states exist at room temperature.

In an attempt to prepare the material with temperatures of magnetic and ferroelectric orderings high enough but still close to each other we grew diluted semiconductor $Eu_{0.8}Ce_{0.2}Mn_2O_5$ (ECMO) single crystals. A strong coupling between magnetic and polar states in multiferroics-semiconductors can arise at sufficiently high temperatures if charge carriers participate in formation of both the magnetic (through double-exchange interaction[5,6]) and ferroelectric (through charge ordering[7]) long-range orders, which was demonstrated in the investigations of multiferroic-semiconductor $Tb_{0.95}Bi_{0.05}MnO_3$.[8–11] It can hardly be expected that multiferroics with nearly equal and sufficiently high ordering temperatures can be formed in solid solutions of dielectric ferroelectric and ferromagnetic crystals. The interactions responsible for the ferroelectric state in dielectric crystals are typically stronger than the interactions responsible for the magnetic order.

This paper reports on comprehensive studies of x-ray diffraction, heat capacity, dielectric and magnetic properties, and Raman light-scattering spectra of single crystals of $Eu_{0.8}Ce_{0.2}Mn_2O_5$ in which the state with a giant permittivity ($\varepsilon' \sim 10^4$) have been observed above 185 K. It has been found that the nature of the high-temperature state in ECMO differs from that of the low-temperature ($T \leq 40$ K) improper ferroelectricity in the initial $EuMn_2O_5$ (EMO) crystals related to a complicated magnetic structure.[1–4] Electron doping with Ce^{4+} ions that substitute Eu^{3+} ions produces charge carriers, and the ratio between Mn^{3+} and Mn^{4+} concentrations changes during crystal growth. As a result, the character of charge ordering typical of initial nondiluted crystals with equal Mn^{3+} and Mn^{4+} concentrations changes.

The state of phase separation into conductive ferromagnetic and dielectric antiferromagnetic domains typically observed in magnetic semiconductor $La_{1-x}A_xMnO_3$ (A=Sr, Ca, Ba) (Refs. 5 and 6) occurs in magnetic semiconductor-multiferroic ECMO as well. However, the symmetry of this phase separation in our crystal is different. Manganese ions Mn^{3+} and Mn^{4+} in EMO are arranged in neighboring atomic layers normal to the *c* axis. The layered arrangement of manganese ions is preserved at crystal doping, but the Mn^{3+} concentration becomes higher than that of Mn^{4+}. Phase separation and charge self-organization result in new ferroelectric and magnetic states in ECMO at all temperatures.

We present here investigations of dielectric properties and heat capacity at low temperatures which have shown that phase transitions characteristic of the initial crystal but somewhat modified by doping are observed in the doped crystal.

This indicates that the major doped crystal volume at low temperatures is occupied by the initial undoped crystal, and only a small volume is modified by doping. This small volume is comprised of as-grown two-dimensional (2D) semiconductor superlattices normal to the c axis and containing doping impurities, charge carriers, and ferromagnetic Mn^{3+}-Mn^{4+} ion pairs. These superlattices appreciably change the processes of magnetization and dielectric relaxation in doped crystals as compared with initial crystals.

At high temperatures ($T>185$ K), a layered superstructure is formed in the doped crystal. A periodic alternation of charged and dielectric layers gives rice to the state of ferroelectricity due to charge ordering with a giant permittivity. It has been found that if a sufficiently high magnetic field is applied at a low temperature, a polarized state is formed at a higher temperature than at $H=0$. This state is metastable and long living. Note that earlier a highly polarized state that changed on application of a magnetic field in an irreversible manner was observed in a diluted multiferroic $Tb_{0.95}Bi_{0.05}MnO_3$.[9,11] Frequency conductivity dispersion was found to exhibit different behavior for the magnetic field oriented along and transverse to the quasi-2D layers.

An influence of the self–organization and ferroelectricity related to charge ordering on Raman-scattering spectra of ECMO have been studied. The paper includes Secs. I–VI.

II. EXPERIMENTAL TECHNIQUES AND THE OBJECT OF STUDY

Single crystals of ECMO were grown by the flux method using the same technology as for the initial EMO crystals.[12] The crystal symmetry and composition were determined by x-ray phase analysis and the x-ray fluorescent method, respectively. In addition the intensity distributions of Bragg reflections for EMO and ECMO crystals were carried out with a high-sensitivity three-crystal x-ray diffractometer. The ECMO symmetry at room temperature did not differ from that of the initial EMO crystals (space group *Pbam*). The unit-cell volume varied only slightly at doping. The lattice constants of ECMO were: $a=7.44\pm0.01$ Å, $b=8.42\pm0.01$ Å, and $c=5.71\pm0.01$ Å, while for EMO they were $a=7.4003$ Å, $b=8.5663$ Å, and $c=5.6972$ Å.

Ions in RMn_2O_5 crystals lie in the layers normal to the crystal c axis.[2] R^{3+} ions are in the $z=0$ layers and have surrounding (RO_8). Mn^{4+} ions ($t_{2g}^3e_g^0$) are in the $z=0.25$ c and $(1-z)=0.75$ c layers and have octahedral surrounding (MnO_6). The octahedra with common apical oxygen ions are elongated along the c axis and form ribbons. Jahn-Teller Mn^{3+} ions ($t_{2g}^3e_g^1$) lie in the $z=0.5$ c layers in pyramids formed by five oxygen ions (MnO5).

A variable valence of $Ce^{3.75+}$ ions is typically realized in cerium-containing crystals. The Ce^{4+} ion radius is smaller than that of Ce^{3+} [1.11 and 1.28 Å, respectively, at coordination number $Z=8$ (Ref. 13)]. The Eu^{3+} ion radius is 1.21 Å.[13] In view of a smaller size of Ce^{4+} ions and also the data of Ref. 14, it can be supposed that the main doping ion in the crystals studied is Ce^{4+}. Note that in Ref. 14, along with studies of valence manganese ions in ceramic $Bi_{0.9}Ce_{0.1}Mn_2O_5$ samples, ferromagnetic ordering below 40 K and two types of dielectric relaxation processes were reported. Doping results in a free electron ($R^{3+}=Ce^{4+}+\mathbf{e}$). Free electrons in ECMO propagate in the subsystem of manganese ions, which is typical of manganites.[5,6] The nearest neighbors of the layers with R^{3+} and Ce^{4+} ions are those with Mn^{4+} ions. The free electrons in the Mn^{4+} layer provide recharging $Mn^{4+}+\mathbf{e}\leftrightarrow Mn^{3+}$. Thus, doping impurities and charge carriers in ECMO are located in neighboring atomic layers perpendicular to the crystal c axis.

Dielectric measurements of capacity and conductivity were carried out with a Good Will LCR–819 impedance meter in the temperature interval 5–350 K and frequency range 250 Hz–100 kHz. The dc-current conductivity σ_{dc} and the ac-current conductivity σ_{ac} were measured by four-contact and capacity methods, respectively. Dielectric spectra were recorded with a Newtons 4th Ltd PSM 1735 device at frequencies 100 Hz–5 MHz in the temperature range 120–300 K. Capacitors in the form of ~0.5-mm-thick plates cut from the single crystals perpendicular to the principal crystal axes were used. Contacts were made by gold evaporation.

Raman-scattering spectra were investigated with a T64000 (Joben Ivon) triple spectrophotometer by using a charge coupled device camera cooled with a liquid nitrogen. A microscope was introduced into the optical scheme. Light was excited with an argon laser at $\lambda=514.5$ nm and was scattered in the 180° geometry. The same ECMO samples were used for Raman and x-ray investigations.

Heat capacity was measured by a physical properties measurement system (Quantum design) at temperatures ranging from 2 to 315 K. The magnetic moment of ECMO was measured with a vibration magnetometer in magnetic fields up to 35 kOe oriented along the a and c crystal axes.

III. X-RAY DIFFRACTION STUDIES

Diffraction studies were performed for several samples of ECMO and EMO at room temperature. The angular intensity distribution of $(\mathbf{004})_{CuK\alpha1}$ Bragg reflections was detected in the three-crystal regime with the $(\Theta-2\Theta)$ scan having a resolution of $\approx10''$. The half-width of the rocking curve (ω_Θ) for one of the Bragg peaks was measured in the (Θ-scan) regime, and the lattice constant (d) was inferred from the Bragg angle Θ_B of this peak. As a monochromator and an analyzer, germanium crystals in the (004) reflection were used, which allowed conditions of nearly dispersion-free high-resolution survey geometry to be realized.

Figs. 1(a) and 1(b) show diffraction curves for ECMO and EMO, respectively. The curve for ECMO [Fig. 1(a)] exhibits a set of diffraction maxima separated into two pronounced regions. Each region has five to six peak pulsations, one of which is dominating in intensity. Both regions have similar widths and number of maxima. Analysis of the diffraction curve has led to the conclusion that the natures of the maxima are different. There are layer peaks whose positions are determined by parameter ($\mathbf{d}$) and which characterize the layered crystal structure. The distances between the maxima ($\Delta\Theta$) of these peaks give information on the lattice mismatch in the layers. In addition, the diffraction curve exhibits periodic intensity oscillations with the $\mathbf{d}$-independent period. All

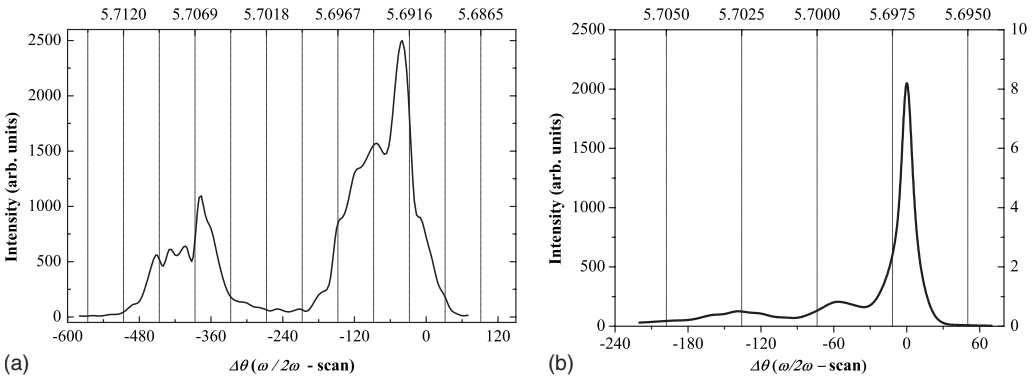

FIG. 1. Angular distribution of Bragg $(004)_{CuK\alpha 1}$ reflection intensity for ECMO (a) and EMO (b) crystals.

five intensity maxima in the left-hand region of the diffraction curve are layer peaks, while only two maxima in the right-hand region are layer peaks, the remaining peaks being oscillatory. The oscillation period ($\Delta\Theta$) is determined by the structural layer thicknesses ($t=\frac{\lambda}{\Delta\Theta\cdot 2\cos\Theta_B}$, where λ is the wavelength). In the right-hand region of the curve $\Delta\Theta=30''$, and the layer thickness is $t\approx 750$ Å. In the left-hand region the layer thicknesses are smaller. The half-width of the rocking curve (ω_Θ) for the layer with the highest peak in the right-hand region is $\approx 20''$, which points to a high structural layer quality.

Fig. 1(b) shows the diffraction curve for EMO. It consists of one intense narrow peak pointing to a high-quality crystal structure in the bulk ($\omega_\Theta=12''$) and two weak broad peaks with oscillations pointing to the presence of a two-layer deformed area at the crystal surface. The layer thickness corresponding to the oscillation period ($\Delta\Theta=23''$) is $t\approx 900$ Å. Thus, room-temperature x-ray studies of the undoped EMO and doped ECMO crystals have shown that the former has a single-crystal structure with a weak layer inhomogeneity in the near-surface area and the latter has a layered superstructure. Note that studies of (060) and (400) reflexes of ECMO have shown their similarity to the (004) reflex for EMO, i.e., each of them has an intense narrow peak and a set of weak broad peaks with oscillations for near-surface region. Thus, room-temperature x-ray studies of the undoped EMO and doped ECMO crystals have shown that the former has a single-crystal structure with a weak layer inhomogeneity in the near-surface area and the latter has a layered superstructure.

IV. LOW TEMPERATURES

A. Dielectric properties

Figs. 2(a)–2(c) presents dielectric properties of ECMO crystals at low temperatures. As can be seen from the inset to Fig. 2(c), the temperature dependence of the real part of permittivity ε' of undoped EMO exhibits maxima in the vicinity of 20 and 35 K when the ac-electric field (**E**) is along the a and b axes. At $\mathbf{E}\|c$ there are no anomalies. A sharp maximum at $T\approx 35$ K corresponds to a ferroelectric phase transition.[12,15] Note that the ε' magnitudes for the initial and doped crystals at low temperatures are nearly equal.

No distinct ε' maxima are observed for doped ECMO. However, for $\mathbf{E}\|b$ [Fig. 2(b)] there is a broad ε' maximum without frequency dispersion at $T\approx 30$ K attributable to the ferroelectric phase transition similar to that observed in EMO at almost the same temperature. This indicates that the major doped crystal volume is occupied by the initial EMO and only a small volume of the crystal modifies by doping.

At $\mathbf{E}\|a$ [Fig. 2(a)], there is no even a diffuse ε' maximum at $T\approx 30$ K. However, relaxation processes with frequency dispersion are observed above 20 K. They manifest themselves as ε' steps and dielectric dissipation maxima $\tan\delta$ ($\tan\delta=\frac{\varepsilon'}{\varepsilon''}$, ε'' is the imaginary part of permittivity).

At $\mathbf{E}\|c$ [Fig. 2(c)], the $\varepsilon'(T)$ dependences are nearly linear in a wide temperature range below 100 K with a change in slope at $T\approx 40$ K. The permittivity ε' is frequency dependent: the higher the frequency, the lower the ε' magnitude. Note that ε' has similar frequency dependence for all **E** orientations.

It is natural to attribute the differences in dielectric properties of the initial and doped crystals to the effect of doping. As noted above, at low temperatures only a small doped crystal volume is occupied by the doped crystal occupies by the as–grown 2D layers normal to the c axis. These layers differ in the number of atomic layers, concentrations of doping impurities and charge carriers, and barriers at the boundaries and can be regarded as one-dimensional (1D) semiconductor superlattices formed in the single-crystal bulk. At low temperatures the superlattices interact with each other only slightly, and the number of charge carriers in them is governed by the electroneutrality condition.

When analyzing dielectric properties of the doped crystal, we assume that the dielectric volume of the initial matrix and the 2D layers with charge carriers have the same magnetic and ferroelectric orderings. However, in 2D layers these orderings are frustrated by doping impurities and Mn^{3+}-Mn^{4+} ion pairs. Dielectric and magnetic measurements and also neutron-scattering data[15,16] have shown that the sequence of phase transitions in EMO is as follows: magnetic phase transition with $T_N\approx 40$ K, ferroelectric phase transition with $T_C\approx 35$ K, and phase transition in the vicinity of 20 K. Below T_N magnetic ordering with wave vector $\mathbf{q}=[1/2,0,\tau]$ with $\tau=0.3$ occurs; i.e., there is an antiferromagnetic ordering along the a axis and incommensurate magnetic structure along the c axis. The ferroelectric phase transition in EMO

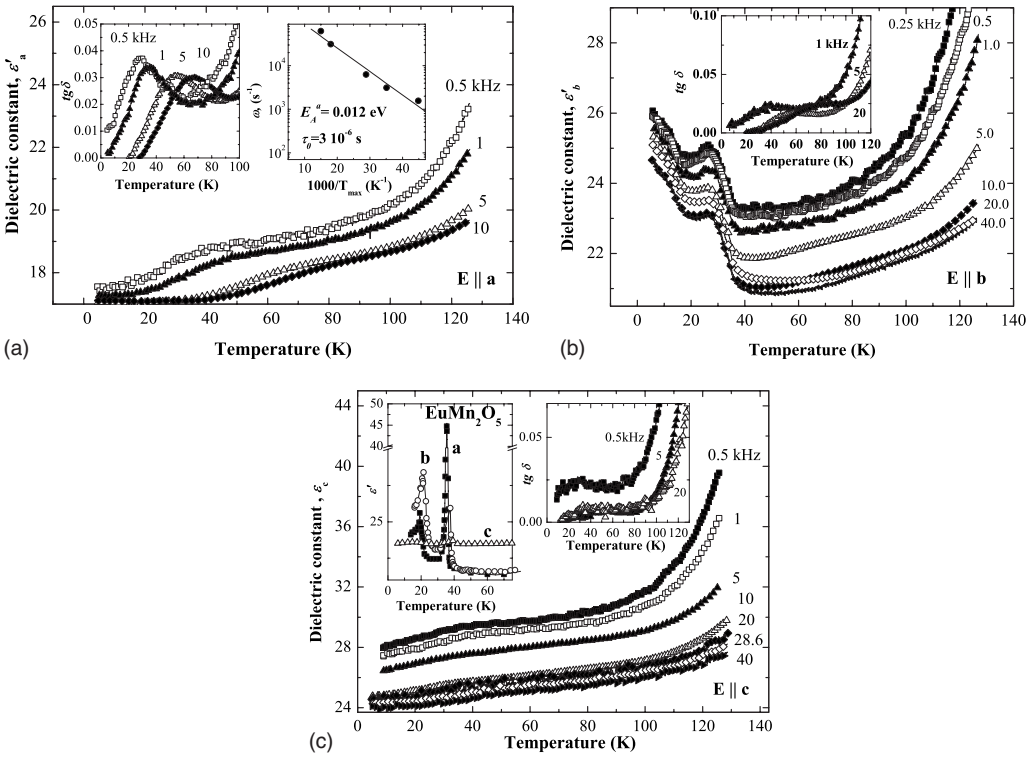

FIG. 2. Temperature dependences of the real part of permittivity ε' for a number of frequencies (kHz) indicated near the curves for different orientations of the ac-electric field (a) $\mathbf{E}:\mathbf{E}\|a$, (b) $\mathbf{E}\|b$, and (c) $\mathbf{E}\|c$. Left inset to Fig. 2(a): temperature dependences of dissipation factor tan δ for a number of frequencies (kHz) indicated near the curves. Right inset to Fig. 2(a): Arrhenius law for the temperatures of dissipation factor maxima. Inset to Fig. 2(b): temperature dependences of tan δ for a number of frequencies (kHz) indicated near the curves. Left inset to Fig. 2(c): temperature dependences of ε' along the a,b,c crystal axes at 1 kHz for EMO. Right inset to Fig. 2(c): temperature dependences of tan δ for a number of frequencies (kHz) indicated near the curves.

arises somewhat below T_N. The polarization vector is oriented along the b axis. In the vicinity of the ferroelectric transition temperature the magnetic structure wave vector changes in a jump. At lower temperatures the wave vector $\mathbf{q}=[1/2,0,1/3]$, i.e., the magnetic structure becomes commensurate.[16] A lower-temperature phase transition near 20 K is simultaneously structural and magnetic.

The relaxation processes of ECMO manifest themselves in the most pronounced way at $\mathbf{E}\|a$. These processes can be attributed to displacements of the charge carriers responsible for recharging of Mn^{3+}-Mn^{4+} ion pairs inside the 2D layers. This results in a phase separation into conductive ferromagnetic and dielectric antiferromagnetic domains. The phase separation is caused by double exchange (exchange interaction between neighboring Mn^{3+} and Mn^{4+} ions through $\mathbf{e}_g$ electrons) described by a Hamiltonian

$$H_J = -J\cos(\psi/2)S_1S_2. \tag{1}$$

Here, ψ is the angle between the directions of localized spins S_1 and S_2 of neighboring Mn^{3+} and Mn^{4+} ions, and J is an exchange constant ($J\sim 300$ meV). Such an exchange gives rise to a ferromagnetic S_1 and S_2 orientation and charge carrier accumulation in the ferromagnetic domains.[5,6] Thus, the relaxation processes inside the 2D layers at $\mathbf{E}\|a$ are accompanied by phase separation. The maxima in tan δ satisfy the condition $\omega\tau=1$ for conductive ferromagnetic domains of different sizes (here ω is the frequency and τ is the domain lifetime). The frequency dependence of the temperatures of tan δ maxima obeys the Arrhenius law [see Fig. 2(a)]

$$\tau = \tau_0\, exp\left(\frac{E_A^{rel}}{kT_{max}}\right) \tag{2}$$

where τ_0 and E_A^{rel} are the lifetime and characteristic activation barrier, respectively. In our case $\tau_0\approx 10^{-6}$ s and $E_A^{rel}\approx 12$ meV. The charge carrier displacements in the layers are hindered by the antiferromagnetic indirect exchange interaction leading to an antiferromagnetic orientation of manganese ion spins along the a axis [in this case $\cos(\psi/2)=0$ in Eq. (1)]. $E_A^{rel}\approx 12$ meV corresponds to the magnitude of the indirect antiferromagnetic exchange. We suppose that a high $\tau_0\approx 10^{-6}$ s is due to a low probability of the conductive domain decay as a whole.

At $\mathbf{E}\|b$, the distribution of the barriers hindering charge displacements in the layers is mainly due to ferroelectric ordering. Above 35 K, the barriers are determined by the interfaces between the domains of ferroelectric correlations which are preserved to the temperatures well above 35 K.[17]

At $\mathbf{E}\|c$, ε' is determined by the charge carrier displacements between the layers and, hence, the barriers at their boundaries. The frequency dependence of ε' for all crystal orientations in a wide temperature interval below 100 K is due to the presence of layers and conductive domains in

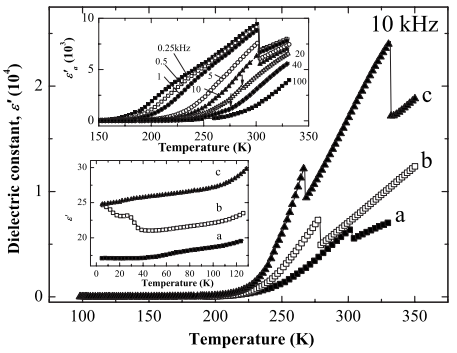

FIG. 3. Anisotropy of $\varepsilon'_{a,b,c}$ for ECMO at 10 kHz. The lower inset: the same for low temperatures. The upper inset: temperature dependences of ε' at $\mathbf{E}\|a$ for ECMO at some frequencies indicated near curves.

them. The layer response depends on the layer size. As frequency grows, responses from thinner layers or smaller domains inside the layers are detected. The thinner the layer, the higher the activation barrier at its boundary and the higher the carrier concentration in it. Charge carriers screen polarization and reduce ε'. The lower inset to Fig. 3 shows anisotropy in ε' at low temperatures. It can be seen that the minimal ε' is observed along the a axis. At $\mathbf{E}\|c$ the magnitude of ε' is the highest.

Let us now consider the effect of magnetic field ($\mathbf{H}\|a$, $H=6$ T) on the relaxation in ECMO at low temperatures. It can be seen from Fig. 4 that the relaxation processes are preserved as the field is applied but anomalies in ε' and tan δ shift towards higher temperatures. In addition, these anomalies are more diffuse and their magnitudes are lower than those at $H=0$ (see inset to Fig. 4). A characteristic activation barrier in the Arrhenius law of 12 meV at $H=0$ becomes equal to 78 meV. As before, we attribute the observed low-temperature relaxation in magnetic field to phase separation inside the quasi-2D layers. The magnetic field $\mathbf{H}\|a$ increases the sizes of the conductive ferromagnetic domains in the layers and enhances the barriers at the boundaries between these domains and dielectric antiferromagnetic domains due to double exchange.

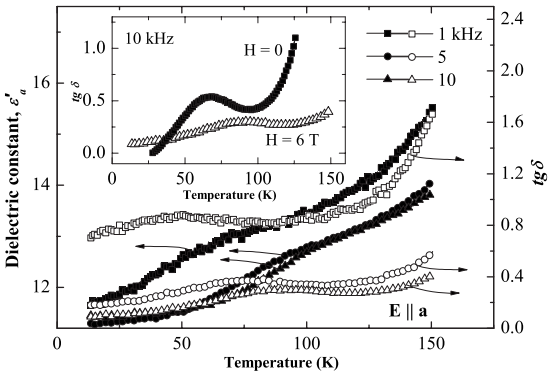

FIG. 4. Temperature dependences of ε' and tan δ for ECMO at $\mathbf{E}\|a$ for the several frequencies. Magnetic field $H=6$ T, $\mathbf{H}\|a$ was applied at 5 K and the sample was heated under the magnetic field. The inset compares temperature dependences of tan δ at $\mathbf{E}\|a$ in zero and nonzero magnetic fields. Frequency is 10 kHz.

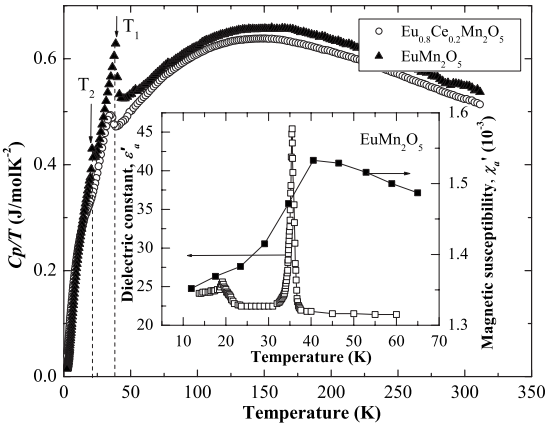

FIG. 5. Temperature dependences of C_p/T for EMO and ECMO. The inset shows temperature dependences of permittivity ε' at $\mathbf{E}\|a$ and magnetic susceptibility χ along the a axis for EMO.

B. Specific-heat results

This section is concerned with studies of heat capacities of EMO and ECMO single crystals. Figure 5 shows temperature dependences of C_p/T for EMO and ECMO exhibiting two anomalies. For EMO these are pronounced anomalies in the vicinity of $T_1 \approx 39$ K and $T_2 \approx 21$ K. Note that earlier[18] a distinct anomaly near 40 K and a weak anomaly near 20 K were reported for heat capacity of EMO. The temperature dependence of C_p/T for ECMO has anomalies shifted towards lower temperatures: a diffuse anomaly in the vicinity of 34 K and a bend in vicinity of 15 K (Fig. 5). Nearly equal temperatures at which anomalies in the temperature dependence of C_p/T of the doped and initial crystals are observed confirm the conclusion that the major doped crystal volume contains the initial crystal state and its small volume is modified by doping. Let us remind that the studies of the low-temperature dielectric properties also pointed to this fact (see Sec. IV A).

Note that the anomaly in the temperature dependence of C_p/T of EMO at $T_1 \approx 38.9$ K does not coincide exactly with either T_N or T_C. Probably we observed a combined response of the system to two phase transitions occurring at close temperatures. This feature distinguishes EMO from other crystals of the $R\mathrm{Mn_2O_5}$ (R=Tb,Dy,Ho) family where anomalies in heat capacity were observed in the vicinity of each of phase transitions.[19]

As noted above, the displacement of the C_p/T anomaly at T_1 toward lower temperatures and its smoothing for ECMO as compared with EMO (see Fig. 5) can be caused by two factors, i.e., a decrease in the magnetic ordering temperature and suppression of critical fluctuations by the quasi-2D layers. Suppression of critical fluctuations reduces entropy and decreases C_p/T near T_1. The layers contain ferromagnetic Mn^{3+}-Mn^{4+} ion pairs which decrease the internal effective field responsible for magnetic ordering of the initial crystal matrix, which reduces T_1. In addition, these layers have structural distortions caused by excess Jahn-Teller Mn^{3+} ions which suppress fluctuations in the vicinity of the ferroelectric transition. Such a behavior of heat capacity near the Neel point was observed earlier at doping of multiferroics

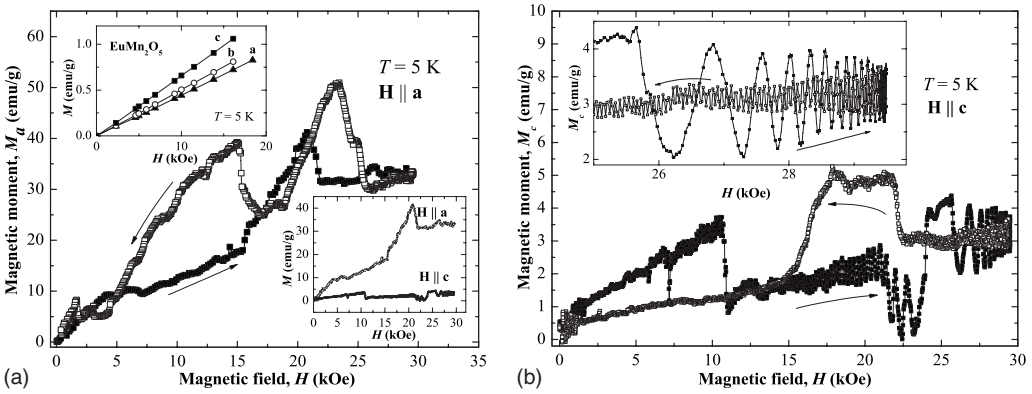

FIG. 6. Magnetic moment as a function of magnetic field for ECMO. $T=5$ K. $\mathbf{H} \| a$ (a) and $\mathbf{H} \| c$(b). The arrows show the directions of field variations. Upper inset to Fig. 6(a): magnetic moment as a function of magnetic field oriented along the principal axes of EMO. $T=5$ K. Lower inset to Fig. 6(a): anisotropy of magnetic moment with increasing field for ECMO. Inset to Fig. 6(b): oscillations of magnetic moment in high magnetic fields.

$YMn_{1-x}Ga_xO_3$ and $HoMn_{1-x}Ga_xO_3$ (Ref. 20) and was attributed by the authors to the nonmagnetic dilution of magnetic ions by doping impurities and a reduction in the magnetic entropy in the critical region.

A narrow anomaly observed in EMO in the vicinity of 21 K displaces at doping towards lower temperatures and becomes a bendlike anomaly. As a result, C_p/T of the doped crystal at low temperatures becomes higher than that of EMO (Fig. 5).

C. Magnetization processes

Let us consider magnetization of the doped crystal along and transverse to the superlattice layers and compare it with magnetization of EMO. It can be seen from Fig. 6 that magnetization curves of ECMO radically differ from those of EMO. The magnetization curves for EMO were found to be linear for the magnetic field orientations along all crystal axes [see the upper inset to Fig. 6(a)].[15] The magnetic moments along all axes in EMO are considerably lower than in ECMO. The magnetic moment along the a axis is the lowest, and that along the c axis is the highest. At $\mathbf{H}=0$ the residual magnetic moments are zero.

It can be seen from Fig. 6 that the magnetic moments in the doped crystal are much higher than those in the initial crystal in all crystal directions. In spite of this fact the data for the doped crystal are fluctuating widely and more noisy than those for EMO. ECMO exhibits a strong magnetic anisotropy the character of which differs from that of the initial crystal. The magnetic moment along the a axis is much higher than that along the c axis. The magnetization curves are nonlinear and have jumps at some magnitudes of magnetic fields oriented both along the a and c axes. The magnetization behavior along the c axis changes irreversibly in the processes of magnetic field cycling and oscillations appear in the third cycle [Fig. 6(b)].

The oscillation period changes abruptly at the jump of the magnetization near $H=25$ kOe. This jump in magnetization one can relate to a magnetic phase transition. When the field decreases down to $H \sim 25$ kOe the oscillation period is constant and equal to the value observed at the highest field. This points to irreversible influence of the magnetic field on the properties of the crystal. We will show below that if the field stronger then 25 kOe is applied at $T=5$ K along the c axis, irreversibility manifest itself also in the dielectric properties of the crystal.

Let us discuss the magnetization curves of the doped crystal in more detail. As the magnetic field oriented along the a axis increases, a linear $M(H)$ dependence with a zero magnetic moment at $\mathbf{H}=0$ is observed under low fields ($\mathbf{H}<5$ kOe). In the field interval 5–17 kOe the magnetic moment decreases thus deviating from the linear $M(H)$ dependence. At $\mathbf{H}>17$ kOe, the magnetic moment begins to grow sharply again and exhibits a maximum at $\mathbf{H} \approx 21$ kOe. As the field further increases, the magnetic moment becomes saturated and fairly high; i.e., it exceeds by a factor of 40 the magnetic moment of EMO (in the same magnetic field). There is a hysteresis as the field decreases.

We believe that a considerable difference between magnetic properties of the doped and initial crystals is caused by the existence of superlattices. The magnetic system of ECMO consists of localized manganese ion spins and the charge carrier spins providing recharging of Mn^{3+}-Mn^{4+} ions in the 2D layers. Localized manganese ion spins have a positive magnetic susceptibility, while the magnetic susceptibility of free charge carriers in the 2D layers can be negative. The negative susceptibility results from rotation of free charge carriers in the layers around the field applied normal to the layers, their orbital states being quantized in the magnetic field (Landau diamagnetism). Charge carriers can be free in the 2D layers if the spins of the Mn ions are ferromagentically aligned in these layers.

If $\mathbf{H} \| a$, the linear $M(H)$ dependence for ECMO [Fig. 6(a)] at ($\mathbf{H}<5$ kOe) results mainly from the predominant contribution of localized manganese ion spins. This is a weak longitudinal antiferromagnetic susceptibility of the dielectric antiferromagnetic phase. This contribution into the magnetic moment is the same for the initial and doped crystals. The major contribution into the magnetic moment of the doped crystal comes from a high positive ferromagnetic susceptibility of Mn^{3+}-Mn^{4+} pairs in the 2D layers. As a result, the initial linear $M(H)$ slope for the doped crystals considerably

exceeds that for the initial crystals. The ferromagnetic moment of Mn^{3+}-Mn^{4+} pairs in the 2D layers grows with increasing magnetic field. The phase separation inside the layer leads to formation of ferromagnetic conductive domains. The higher the magnetic field, the larger the domain. In this case the diamagnetic susceptibility caused by rotation of charge carriers normal to the magnetic field (across the layer) is weak. As a result, the total magnetic susceptibility (of localized spins and charge carriers) becomes nonlinear. The sharp jump in the magnetic moment at $\mathbf{H} \approx 21$ kOe is related to the metamagnetic phase transition in the subsystem of localized manganese ion spins in the 2D layers. This transition occurs when the external magnetic field becomes equal to the internal effective antiferromagnetic field. The latter is weakened in the layers with ferromagnetic frustrations. After the metamagnetic transition, a ferromagnetic ordering for all manganese ion spins is established in the layers. As the field further increases, the ferromagnetic moment becomes saturated, and its magnitude is rather high. Therefore, a high magnetic moment in the doped crystal at increasing magnetic field $\mathbf{H} \| a$ is due to the ferromagnetism of localized manganese ion spins in the 2D layers, while the magnetic moment along the a axis of EMO is due to a low longitudinal antiferromagnetic susceptibility.

If $\mathbf{H} \| c$, the magnetic field is along the $[0,0,\tau]$ vector. The modulated long-range magnetic order in the layers is also frustrated by ferromagnetic Mn^{3+}-Mn^{4+} ion pairs. Application of a sufficiently high magnetic field along the c axis leads to formation of a homogeneous magnetic structure along this axis and, first of all, inside the layers. The magnetic moment jump at $\mathbf{H} \sim 25$ kOe is observed. It is likely that a phase transition from the incommensurate phase into a homogeneous magnetic state of manganese ion spins in the layers occurs under this field [Fig. 6(b)]. Note that both the metamagnetic transition at $\mathbf{H} \| a$ and transition at $\mathbf{H} \| c$ are observed in nearly equal magnetic fields. This suggests that the latter transition is the spin–flip phase transition for antiferromagnetically ordered local spins in the layers. It could be expected that ferromagnetic moments in the layers due to local spin orientation would be nearly equal along the a and c axes, but in reality $\mathbf{M}_a \gg \mathbf{M}_c$ [Fig. 6(a)]. Probably, this is due to a high diamagnetic susceptibility of free carriers in 2D layers at $\mathbf{H} \| c$. As a result, the total magnetic moment along the c axis is appreciably reduced, which leads to a strong magnetic anisotropy of the doped crystal.

The increasing magnetic field $\mathbf{H} \| c$ also results in redistribution of the charge carrier concentrations between the 2D superlattice layers, thereby changing the barrier at the 2D layer boundaries, and forming the dynamic equilibrium state of the superlattices. The barrier at the 2D layer boundary can be written as

$$W = W_m + W_{DE} - W_C \tag{3}$$

where W_m is the barrier in the lattice; W_{DE} is the barrier due to the double exchange [Eq. (1)]. The magnetic field, by leading to a ferromagnetic orientation of $\mathbf{S}_1$ and $\mathbf{S}_2$ spins, increases the barrier at the layer boundary by W_{DE}. The Coulomb repulsion W_C is[22]

$$W_C = \frac{e^2}{\varepsilon_0 R_{12}}. \tag{4}$$

Here $\mathbf{e}$ is the electron charge, ε_0 is the permittivity, and R_{12} is the distance between charge carriers. As the concentration of charge carriers in the layers increases, the distances between them decreases, and the Coulomb repulsion that reduces the barrier becomes stronger. As a result, a high enough magnetic field $\mathbf{H} \| c$ forms equilibrium 1D superlattices with a balance between attraction forces (double exchange, Jahn-Teller interaction) and Coulomb repulsion for charge carriers. The superlattices formed in the single-crystal bulk of ECMO due to charge carrier self-organization in a magnetic field are similar to specially prepared semiconductor superlattices (see, e.g., Ref. 23). We believe that magnetic oscillations are excited in sufficiently high magnetic fields $\mathbf{H} \| c$ in the dynamic equilibrium superlattices and they are de Haas–van Alphen (dHvA) oscillations. It is known[21] that the dHvA oscillation frequency F for superlattices (in units of magnetic field) is

$$F = \frac{\pi c \hbar}{e} n = 2.0610^{-7} n. \tag{5}$$

It can be seen that F is determined by the charge carrier concentration n in the layer of the superlattice. Here, c is the velocity of light, e is the electron charge, and $\hbar$ is the Planck constant. In our case the oscillation frequency prior to the phase transition $F_a = 10^6$ Oe, the charge carrier concentration being $n_a = 5 \times 10^{12}$ (cm^{-2}). After the phase transition $F_b = 10^7$ Oe and $n_b = 5 \times 10^{13}$ (cm^{-2}). Obtained values of the oscillation frequencies and charge carrier concentrations are typical for oscillations in semiconductor superlattices.[21]

Note that in our case the dHvA oscillations are excited in the internal field that is a sum of the field due to localized ferromagnetic moments of Mn and an external field. The oscillation period is determined by the internal field. Near the magnetic phase transition (at $H \approx 25$ kOe) the oscillation period abruptly changes. To estimate the charge carrier concentrations the frequency values taken sufficiently far from the phase transition were used.

Irreversibility of the state of the superlattices at decrease of the field we link with the lattice distortions due to the Jahn-Teller effect. They maintain higher barriers at the boundaries of the superlattices and a higher concentration of the charge carriers within them. It is the reason of oscillation period difference between the field going up and down cases.

Fluctuating and noisy character of the dependence of the magnetization on the external field is likely due to dynamic state realized in the superlattices. Continuous jumps of the charge carriers are typical for such state and they preserve a balance of the attractive and repulsive forces (the charge carrier self-organization). For these reasons the magnetic state of the superlattice layers is determined by self-organization.

V. HIGH TEMPERATURES

A. Dielectric properties

As noted above, the room-temperature x-ray diffraction study of ECMO revealed the layered superstructure along the

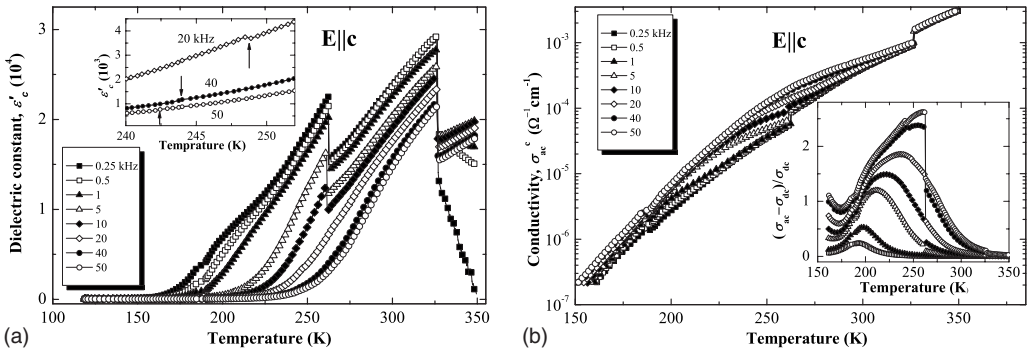

FIG. 7. Temperature dependences of ε' (a) and conductivity σ_{ac} (b) for a number of frequencies (kHz) indicated near the curves, $\mathbf{E}\|c$. Inset to Fig. 7(a): temperature dependences of ε' near 260 K for a number of higher frequencies (kHz). Inset to Fig. 7(b): temperature dependences of local conductivity for a number of frequencies (kHz).

c axis. This means that noninteracting superlattices assumed to be present at low temperatures transform into a layered superstructure throughout the entire crystal volume with increasing temperature.

As can be seen from Figs. 7(a) and 7(b), if $\mathbf{E}\|c$, ε', and σ_{ac} begin to grow above 150 K. At $T\approx 185$ K the $\varepsilon'(T)$ and $\sigma_{ac}(T)$ dependences exhibit anomalies without frequency dispersion, which points to a phase transition at this temperature. Above 185 K, both ε' and σ_{ac} continue to grow and their frequency dispersion increases. The higher the frequency, the higher σ_{ac} and the lower ε'.

The observed frequency dispersion of conductivity is typical of inhomogeneous systems containing domains of different sizes of localized charge carriers with electron correlations.[22] The low-frequency σ_{ac} and σ_{dc} characterize percolation conductivity of the crystal, that has no frequency dispersion. The σ_{ac} with frequency dispersion characterizes local conductivities of small-size domains. These local conductivities are due to ac losses caused by electron transfer between states deep within potential wells of the domains of electron correlations.[22]

Temperature dependences of the local conductivities $(\sigma_{ac}-\sigma_{dc})/\sigma_{dc}$ at different frequencies are shown in the inset to Fig. 7(b). They exist in ECMO in the temperature interval 160–330 K. The frequency shifts of the temperature maxima of local conductivities are described by Arrhenius law (2). The activation barrier for the high-frequency part of these conductivities is $E_A=260$ meV. The temperature interval in which the high permittivity state exists coincides with that of the local conductivity. This means that ε' is mainly determined by the localized charge carriers. Of interest is the presence of jumps on the temperature dependences of $\varepsilon'(T)$ and $\sigma_{ac}(T)$ near 260 K and at $T\approx 325$ K [Figs. 7(a) and 7(b)]. Such jumps are observed with both increasing and decreasing temperature do not show hysteresis phenomena. The first steplike anomalies in the $\varepsilon'(T)$ dependences (near 260 K) exhibit frequency dispersion. The higher the frequency, the lower the jump temperature and the weaker the anomaly [see Fig. 7(a) and the inset to Fig. 7(a)]. As noted above, the lower the frequency, the larger the size of the domain that gives response. At low frequencies there is almost no dispersion of the jumps in both of $\varepsilon'(T)$ and $\sigma_{ac}(T)$ dependences and these jumps occur at $T\approx 262$ K. The dispersive-free anomalies at low frequencies can point to the phase transition at $T\approx 262$ K. It will be shown below (see Sec. V D) the Raman light scattering spectra have an anomaly at the same temperature.

The ε' and σ_{ac} jumps at $T\approx 325$ K do not have frequency dispersion [Figs. 7(a) and 7(b)]. As temperature further grows, ε' drops to nearly zero at low frequencies. At high frequencies ε' continues to grow, probably to have more jumps at higher temperatures. The frequency dispersion of conductivity disappears, i.e., at $T>325$ K percolation conductivity dominates.

Anisotropy of the ε' in the temperature range from ~100 K to ~350 K is presented in Fig. 3. It can be seen that ε' is the highest along the c axis and is the lowest along the a axis. The $\varepsilon'(T)$ dependences along the a and b axes have one jump each (at $T<350$ K), whereas two jumps are observed along the c axis. It is possible that more high-temperature jumps in $\varepsilon'(T)$ along the a and b axes exist at $T>350$ K. Indeed, a frequency dispersion of the jumps in $\varepsilon'(T)$ along the a axis near 300 K is similar to that of the anomalies near 260 K along the c axis (see the upper inset to Fig. 3).

Let us discuss how the state with a giant ε' is formed and what is the nature of the phase transitions observed. At $\mathbf{E}\|c$ [Figs. 7(a) and 7(b)], the hopping conductivity of charge carriers from the as-grown 2D layers increases and the number of carriers in the layers decreases with increasing temperature (at $T>100$ K). The electroneutrality is broken, and the layers become positively charged (owing to doping impurities Ce^{4+}). Due to hops from the as-grown 2D layers, charge carriers (electrons) penetrate into the planes with manganese ions in the dielectric crystal matrix. In these planes recharging $Mn^{4+}+\mathbf{e}\leftrightarrow Mn^{3+}$ takes place, and the layers become negatively charged. Coulomb attraction and annihilation of charged layers is inhibited by the barriers arising at their boundaries due to Jahn-Teller lattice distortions around Mn^{3+} ions. The probability of formation of negatively charged layers in the vicinity of all as-grown layers grows with increasing temperature. We suppose that the phase transition at $T\approx 185$ K corresponds to a percolation phase transition, when an infinite cluster of charged layers alternating with dielectric interlayers of the initial crystal (a layered superstructure) is formed in ECMO.

The layered superstructure arising at $T \approx 185$ K is inhomogeneous and consists of layers with different sizes, charge carrier concentrations, and barriers at their boundaries. This is the reason for appearance of the frequency dispersion in the $\varepsilon'(T)$ and $\sigma_{ac}(T)$. Note that formation of the layered superstructure is accompanied by a change in the lattice state. A periodical distribution of charges in the lattice gives rise to a state of the charge-ordering-induced ferroelectricity with the polarization along the c axis. Application of an ac field $\mathbf{E} \| c$ leads to the barrier height modulation at the layer boundaries and charge displacement from one layer to another. In our opinion, this is the reason for a giant growth in permittivity above 185 K.

The properties of the layered superstructure change above 185 K due to an increase in the probability of hops with increasing temperature. The barriers at the layer boundaries and charge carrier distribution between the superstructure layers at high temperatures are determined by the same interactions as in the superlattices at low temperatures in magnetic field (3), i.e., the electron-phonon, double exchange, and Coulomb interactions. The double exchange makes the barriers at the layer boundaries higher (attraction forces of charge carriers). However, filling of the layers is limited by Coulomb repulsion. The balance between attraction and repulsion charge carrier interactions in the layers gives rice to an abrupt change in the charge carrier concentration. At lower-temperature interval (somewhat above 185 K) the charge carriers are mainly concentrated in the layers with maximal boundary barriers. These barriers are typical of the thinnest layers giving response at higher frequencies. The balance between attraction and repulsion forces of charge carriers occurs for such layers earlier. As s result, weaker jumps in permittivity are observed at lower temperatures and at higher frequencies [see the inset to Fig. 7(a)]. As temperature increases the balance between attraction and repulsion forces of charge carriers is established in the larger domains. In this case the jumps with higher magnitudes occur at lower frequencies and at higher temperatures. The larger the domain size, the weaker the frequency dispersion. At last, frequency dispersion for jumps disappeared at low frequencies. We can assign the low-frequency dispersion-free anomalies at $T \approx 262$ K to phase transition of the dynamic homogeneous state formation in the whole crystal. As temperature further grows, the superstructure decay and percolation conductivity growth start. We suppose that at 325 K the infinite cluster of the layered superstructure is destroyed. At $T > 325$ K localized carriers are preserved only in the small-size isolated clusters formed from the layers with the highest barriers [see Figs. 7(a) and 7(b)].

Let us turn now to the permittivity anisotropy. As evident from Fig. 3, a considerable growth in ε' along all principal crystal axes starts above 150 K, and it is due to enhancement of hopping both inside and between the 2D layers. The anomalies in ε' and σ_{ac} at $T \approx 185$ K corresponding to the percolation phase transition are observed at all crystal orientations. Indeed, a layered superstructure can arise along one of the crystal axis (c axis) in an infinite crystal alone. In a finite-size sample, an edge layer structure along the a and b axis directions also arises. The ε' anisotropy in the samples is determined by the barrier anisotropy at the layer boundaries of the superstructure (see also Sec. V B). The barriers along the c axis are minimal and they are reduced by the internal electric field originating from the ferroelectricity along this axis. By analogy with the phase transition at $T \approx 262$ K (for the c axis), the ε' jumps at higher temperatures along the a and b axes can be attributed as the phase transitions associated with the formation of the edge dynamic equilibrium superstructure (see the upper inset to Fig. 3).

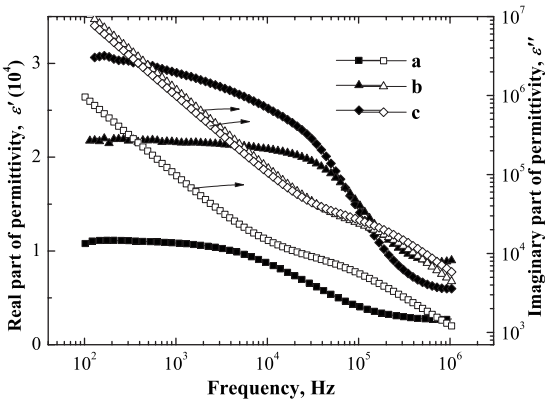

FIG. 8. Frequency dependences of the real (ε': left-hand axis) and imaginary (ε'': right-hand axis) parts of permittivity at room temperature for $\mathbf{E} \| a, b, c$.

B. Dielectric spectra

Figure 8 shows room-temperature dielectric spectra of ECMO for **E** oriented along principal crystal axes. The anisotropy observed is similar to that presented in Fig. 3. There are abruptly falling ε' dependences at definite frequencies typical of Debye relaxation. However, the ε'' maxima typically accompanying Debye relaxation jumps in ε' appear only slightly. This indicates that not only Debye relaxation is responsible for dielectric losses in ECMO. As a rule, such a behavior of ε'' points to a contribution of conductivity into dielectric losses.

As shown in Ref. 22, in semiconductors with random disorder and glasses with a wide range of restricted domains of variable scales with electron correlations, the contribution of conductivity of the domains into dielectric losses is described by Debye relaxation for all frequencies. On the other hand, the layered dielectrics containing layers with different conductivities and permittivities are characterized by dielectric losses described by Maxwell-Wagner relaxation. The dielectric spectra for the case of Maxwell-Wagner relaxation are[24,25]

$$\varepsilon' = \varepsilon_\infty + \frac{\varepsilon_0 - \varepsilon_\infty}{1 + \omega^2 \tau^2}, \tag{6}$$

$$\varepsilon'' = \frac{\sigma}{\omega} + \frac{(\varepsilon_0 - \varepsilon_\infty)\omega\tau}{1 + \omega^2 \tau^2}, \tag{7}$$

where $\sigma = \frac{1}{C_0(R_1+R_2)}$ is the specific σ_{ac}; C_0 is the geometrical factor of the sample; R_1 and R_2 are the layer resistances; and

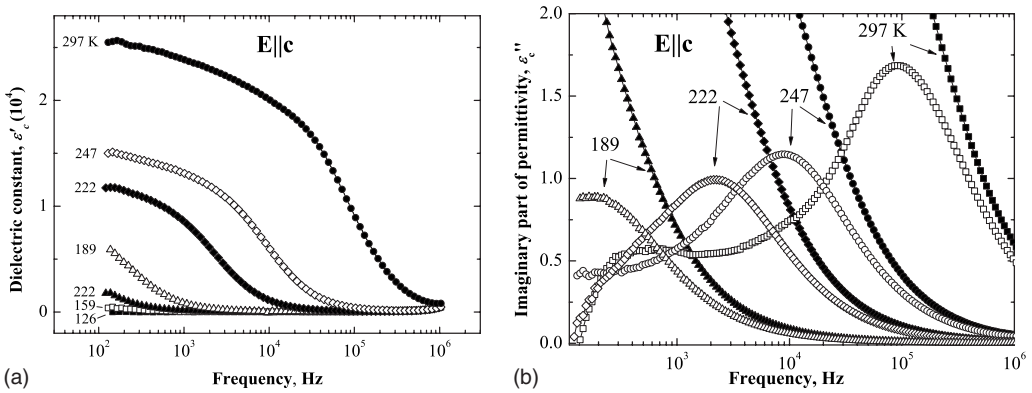

FIG. 9. Frequency dependences of (a) ε' and (b) ε'' for a number of temperatures (kelvin) indicated near the curves. $\mathbf{E}\|c$.

τ is the relaxation time for the layered sample. Equation (6) for ε' is the same for Debye and Maxwell-Wagner relaxations. The equation for the imaginary part of permittivity differs from that for the Debye relaxation by only an additional term associated with conductivity [the first term in Eq. (7)]. It can be seen that this term is the highest at low frequencies, while the contribution of Debye relaxation at low frequencies is the lowest: $\varepsilon'' \to 0$, when $\omega \to 0$. Figures 9(a) and 9(b) present dielectric spectra of ECMO at fixed temperatures for $\mathbf{E}\|c$. The ε' spectra exhibit the behavior typical of Debye relaxation, ε' decreasing abruptly with temperature. These data are in good agreement with Fig. 7(a). Figure 9(b) shows two curves, i.e., the summary ε'' and maxima in ε'' obtained by subtracting σ (obtained from the slope of the linear dependence of summary ε'' on inverse frequency) from the summary ε''. In this case the ε'' maxima typical of Debye relaxation manifest themselves. The frequency shifts of the temperatures of ε'' maxima are well described by Arrhenius relation [Eq. (2)]. The magnitudes of E_A are 260–276 meV, depending on the $\mathbf{E}$ direction. The highest E_A is observed for $\mathbf{E}\|a$, and the lowest E_A is for $\mathbf{E}\|c$. Note that frequency shifts of temperature maxima of localized conductivity in Fig. 7(b) for $\mathbf{E}\|c$ gave the same activation barrier of 260 meV. Note, that the activation barrier anisotropy causes the changing in temperatures of the dynamic homogeneous edge superstructure forming along the crystal axes (see Fig. 3).

Thus, the high-frequency part of localized conductivity is determined by Debye relaxation, and the low-frequency part is determined by Maxwell-Wagner relaxation. In our case the low-frequency part of σ_{ac} and σ_{dc} give contributions into the internal Maxwell-Wagner relaxation caused by the presence of a layered superstructure in the crystal bulk.

C. Effect of magnetic field on dielectric properties

Now we consider the effect of magnetic field on the formation of the layered superstructure state in ECMO. Magnetic field which is high enough to form the equilibrium superlattices is applied at $T=5$ K along the c and a axes. As can be seen from Fig. 10, application of $\mathbf{H}\|c$, $\mathbf{H} \geq 21$ kOe at a low temperature increases the temperature of the highly polarized state formation from 185 to 225 K. In this case ε' grows more abruptly than for $\mathbf{H}=0$. Application of a low magnetic field does not produce any effect. There is a considerable hysteresis for formation of the highly polarized state at sample heating and cooling in a high magnetic field. The cooling curve nearly coincides with the initial (prior to field application) curve. Note that no temperature hysteresis is observed for formation of this state in zero magnetic field (see the inset to Fig. 10). The state with a giant permittivity arising in ECMO at $T>225$ K has a different barrier distribution in the lattice as compared with the state at $\mathbf{H}=0$. A characteristic activation barrier in the Arrhenius law is $E_A \approx 550$ meV (instead of $E_A \approx 260$ meV at $\mathbf{H}=0$). This change in the barrier is comparable to the magnitude of double exchange ($J_{DE} \approx 300$ meV).

The layered superstructure in the doped crystal formed at high temperatures after application of a high magnetic field does not decay when the magnetic field is removed. When the field is removed at a high temperature and the sample is cooled in zero-field cooled (ZFC), the ε' curve, as noted above, is similar to the cooling curve prior to field application. However, when the sample is again heated in zero magnetic field (ZFH), ε' behave as for the heating regime in the magnetic field. Therefore, the metastable but long-living state arises in ECMO after application of a sufficiently high

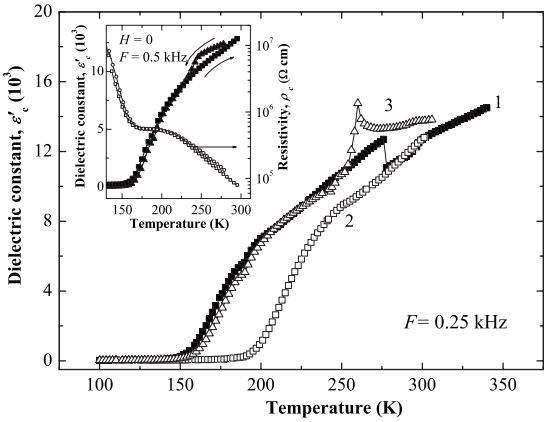

FIG. 10. Temperature dependences ε', $\mathbf{E}\|c$ for the initial crystal state of ECMO in zero magnetic field (curve 1, cooling). Curve 2 is sample heating in magnetic field $\mathbf{H}=6$ T ($\mathbf{H}\|c$) applied at $T=5$ K. Curve 3 is sample cooling (ZFC) after the field is removed at the highest temperature. Frequency is 0.5 kHz. Inset: temperature hysteresis for ECMO prior to magnetic field application.

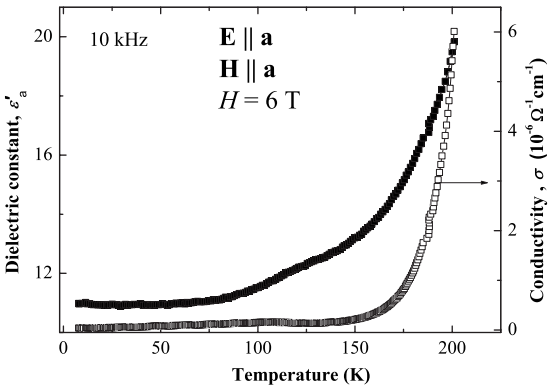

FIG. 11. Temperature dependences of ε' and σ_{ac} for $\mathbf{E}\|a$. Magnetic field $\mathbf{H}=6$ T was applied along the a axis at 5 K and the sample was heated under the applied field. Frequency is 10 kHz.

magnetic field at a low temperature. A slow relaxation (during 15 days) to the initial state (prior to magnetic field application) occurred in our experiments.

Let us now consider the effect of magnetic field applied along the a axis on high-temperature polarized state. Anomalies in ε' and σ_{ac} in the vicinity of 185 K are observed in $\mathbf{H}=6$ T ($\mathbf{H}\|a$, $\mathbf{E}\|a$), like at $\mathbf{H}=0$ and $\mathbf{E}\|c$ (Fig. 11). In accordance with our model, at $\mathbf{H}=0$ and $\mathbf{E}\|c$ a percolation phase transition occurs in the vicinity of this temperature and a layered superstructure along the c axis arises. At $\mathbf{H}=6$ T oriented along the a axis an additional steplike increases in ε' and σ_{ac} somewhat above 185 K are observed (Fig. 12). In our opinion, these jumps occur because the conductive domains inside the layers align parallel to each other and perpendicular to the c axis. Therefore, three-dimensional (3D) domains with the modified layered superstructure along the c axis are formed in the vicinity of 185 K. The volume of this layered superstructure is limited along the a and b axes and consists of a set of 3D domains with different sizes.

It can be seen from Fig. 12 that if the magnetic field $\mathbf{H}=6$ T is applied along the a axis at $T=5$ K and then the sample is heated, the high-temperature highly polarized state

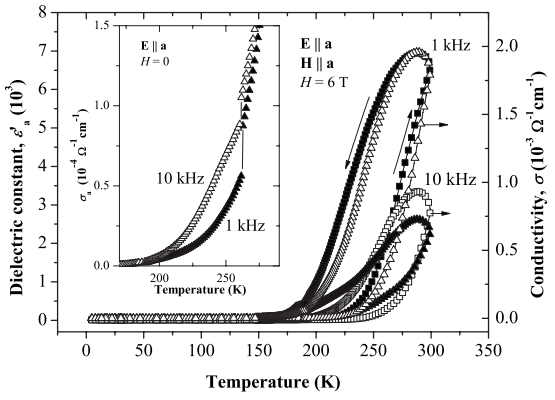

FIG. 12. Temperature dependences of ε' and σ_{ac} for $\mathbf{E}\|a$. Magnetic field $\mathbf{H}=6$ T was applied along the a axis at 5 K and the sample was heated under the applied field. Frequencies are 1 and 10 kHz. The arrows show directions of temperature variations. Inset: temperature dependences of σ_{ac} at $\mathbf{E}\|a$ in the absence of magnetic field at 1 and 10 kHz.

arises in ECMO at higher temperatures than at $\mathbf{H}=0$ and has a hysteresis, similar to the case $\mathbf{H}\|c$ considered above. This state is also metastable and long living. However, there is a qualitative difference in the behaviors of frequency dispersion of conductivity σ_{ac} for $\mathbf{H}\|a$, $\mathbf{E}\|a$, and $\mathbf{H}\|c$, $\mathbf{E}\|c$. For $\mathbf{H}\|c$, $\mathbf{E}\|c$ σ_{ac} grows with increasing frequency [Fig. 7(b)] and for $\mathbf{H}\|a$, $\mathbf{E}\|a$ σ_{ac} decreases with increasing frequency (Fig. 12). In the case $\mathbf{H}\|c$, $\mathbf{E}\|c$ the local σ_{ac} conductivity is due to dielectric relaxation under the layered superstructure barriers. For $\mathbf{H}\|a$, $\mathbf{E}\|a$ σ_{ac} is due to two processes, i.e., displacements of the carriers activated from conductive domains to the dielectric medium of the layers and displacements inside the conductive domains under an applied ac-electric field $\mathbf{E}\|a$. The latter result in a high ε'. The larger the conductive domain inside the layer, the lower the frequency of its response. The charge displacements in larger domains cause higher conductivity and polarizability. Thus, frequency dispersion anisotropy under magnetic fields applied along the a and c axes is also consistent with our model.

D. Raman light scattering

The coexistence of the ferroelectric and magnetic orderings in multiferroics $R\mathrm{Mn_2O_5}$ in the same temperature interval stimulated the use of optical and, first of all, Raman spectroscopy for investigations of their properties[26–28] and for obtaining microscopic information on correlations between spin and phonon states in these crystals. Analysis of Raman-scattering spectra of $R\mathrm{Mn_2O_5}$ has shown that there exist spin-phonon correlations in the vicinity of magnetic and ferroelectric transitions below 40 K and around 60–65 K.[27] Above 185 K, the doped ECMO has a highly polarized state and ferromagnetic correlations. In this section we consider Raman-scattering spectra of ECMO and the influence of self-organization and ferroelectricity due to charge ordering on these spectra.

Figure 13 shows an example of polarized scattering spectra for ECMO. Comparison of experimental Raman spectra of the doped crystal with the spectra of EMO (Ref. 27) has shown that they are similar. Therefore, doping does not radically change the scattering spectrum. This is in line with the x-ray diffraction that points to preservation of the initial space group of the EMO crystal at the present level of doping. According to the theoretical group analysis of the $R\mathrm{Mn_2O_5}$ crystals with the $Pbam$ symmetry, the total number of Raman-active modes must be 48 ($\Gamma_{Raman}=13A_g+13B_{1g}+11B_{2g}+11B_{3g}$).[26,27] In the scattering geometry using the VV polarization (Fig. 13), the most intense modes are the A_g symmetry modes corresponding to the Mn-O stretching vibration. The experiments were carried out in two scattering geometries, with the phonon wave vector ($\mathbf{q}$) directed along the b and c crystal axis, i.e., $Y(XX)Y'$ and $Z(XX)Z'$, respectively. The Raman spectrum intensity in the VH geometry [$Y(XZ)Y'$ and $Z(XY)Z'$] is weak, which makes correct analysis of the spectra difficult. In the case of the VV polarization the mode intensity is high enough to analyze the temperature dependence of frequency. To describe the phonon modes, a damped harmonic oscillator was

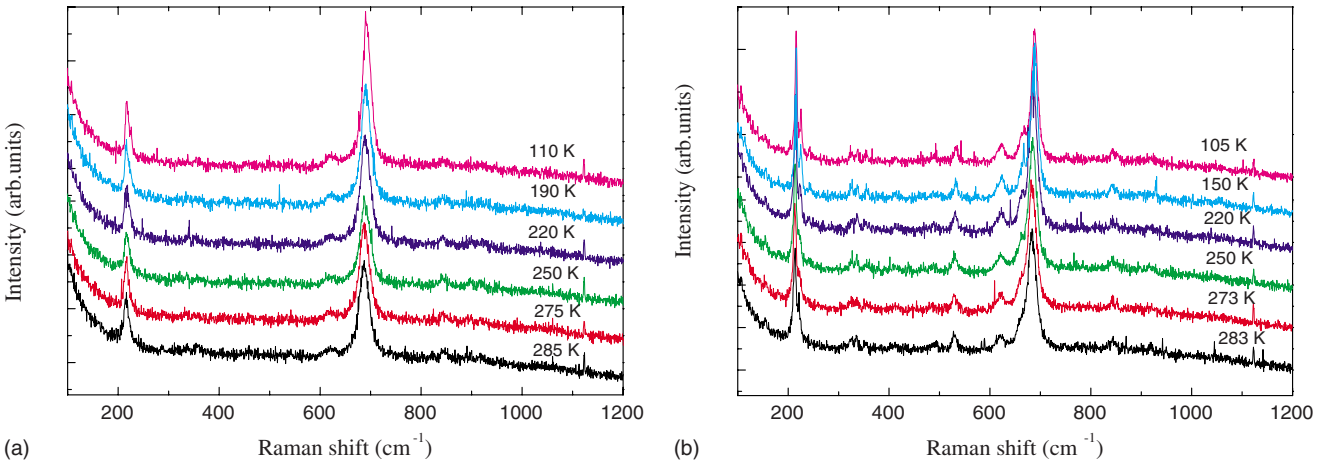

FIG. 13. (Color online) Temperature evolution of Raman spectra obtained in (a) $\mathbf{q}_{ph} \| b$ and (b) $\mathbf{q}_{ph} \| c$ experimental geometries.

used for the fits. We analyzed temperature dependences of the frequency shifts of the A_g modes with $\nu \approx 220$ and ≈ 690 cm^{-1} for both $\mathbf{q}_{ph} \| b$ and $\mathbf{q}_{ph} \| c$ [Figs. 14(a) and 14(b), respectively]. It can be seen from Fig. 14 that the A_g mode frequencies behave similarly in both geometries: at low temperatures, from 80 to ~160 K, the frequency is temperature independent to within the limits of experimental accuracy and starting from ~175 K the frequency begins to decrease linearly with increasing temperature. Note also that changes in frequencies are alike for all the modes considered and are of the order of 0.8% of their initial values. Possibly, an anomaly in the A_g mode frequency occurs in the vicinity of 260 K in the $\mathbf{q}_{ph} \| b$ geometry, but it is too small to speak about it with sufficient certainty. It is natural to attribute the linear decrease in the A_g mode frequencies above 175 K (Fig. 14) to the development of lattice anharmonicity. However, in the absence of structural instabilities such an anharmonic lattice softening is typically observed from the lowest to the highest temperatures. In our case changes in the temperature dependence of mode frequencies begin at fairly high temperatures. The anomalies in the behavior of optical phonons with the A_g symmetry in the vicinity of 175 K correspond to the beginning of growth in permittivity above 180 K [see Fig. 7(a)]. The model of phase transitions in ECMO described above qualitatively explains what lattice dynamics can lead to the absence of temperature dependence of mode frequencies from 80 to 175 K. Indeed, beginning from the lowest temperatures ECMO has noninteracting 2D layers with charge carriers and excess Mn^{3+} concentration. Lattice distortions due to the Jahn-Teller nature of Mn^{3+} ions arise inside these layers and at their boundaries. Since the A_g mode characterizes Mn-O stretching, it is reasonable to suppose that the behaviors of A_g mode frequencies from 80 to 175 K is governed by the coexistence of two competing processes, i.e., local distortions around Mn^{3+} ions and lattice anharmonicity. As noted above, at ≈ 185 K there occurs a percolation phase transition in ECMO and an infinite cluster of the layered superstructure is formed. A new more homogeneous lattice state arises, and the behavior of A_g mode frequencies at $T > 180$ K is mainly determined by crystal anharmonicity.

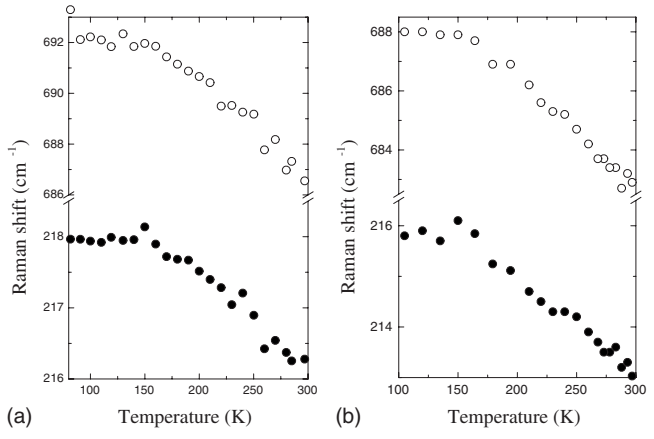

FIG. 14. Temperature dependences of relative changes in frequencies of A_g modes obtained in (a) $\mathbf{q}_{ph} \| b$ and (b) $\mathbf{q}_{ph} \| c$ experimental geometries.

Of interest is the presence of intense polarized quasielastic scattering (QELS) in the low-frequency region at $\nu < 300$ cm^{-1} (see Fig. 15). No similar features have been reported in the literature on Raman scattering in the family of manganites–multiferroics. However, quasielastic scattering was observed in Raman spectra of layered manganites,[29] relaxor ferroelectrics,[30] and other compounds (see, e.g.,[31,32]). The first two compounds are of particular interest for comparison with our crystal. The quasielastic light scattering from layered manganites was attributed to fluctuations in spin density, while quasielastic scattering from relaxor ferroelectrics was attributed to the relaxation mode associated with the dynamics of polar domains of a nanometer size.[33] As shown above, ECMO exhibits the permittivity dispersion in a wide temperature range, such as relaxor ferroelectrics. Such a dispersion points to the presence of restricted domains of permittivity correlations of different scales in our crystal. As will be shown below, there is a correlation between temperature dependences of dielectric properties and behavior of Raman spectra in ECMO, as in relaxor ferroelectrics.

We find that the quasielastic scattering in the low-frequency region of the Raman spectra is well described by the Lorentz function centered at the unshifted frequency.

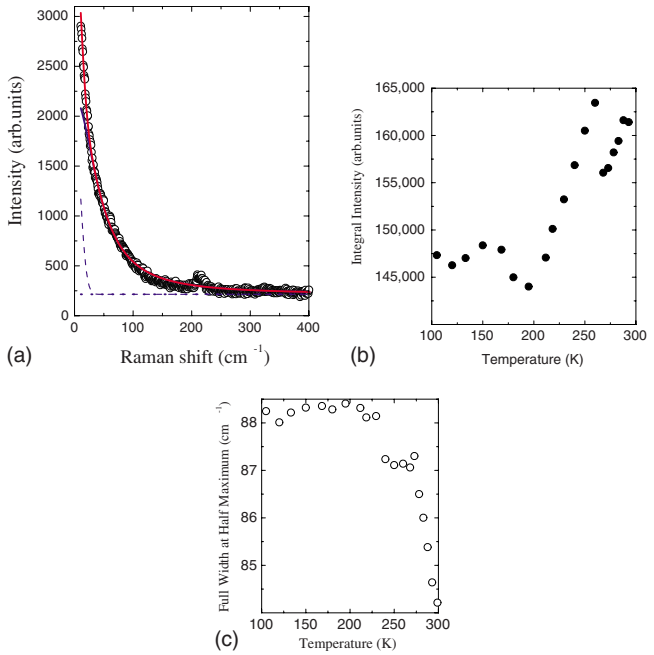

FIG. 15. (Color online) Quasielstic light sattering: a-shows an example of fitting of the low-frequency region of Raman spectrum (the dashed line is a laser line (Gauss function), the dotted line is a background, the solid blue line is a quasielastic scattering (Lorentz function), the solid red line is a result of fitting, and the open circles are experimental data); temperature dependences of integral intensity (b) and full-width at half-maximum (c).

Note that the attempts to describe QELS by the Gauss function or combination of two Gauss functions at different temperatures failed. If we assume that the Lorentz function corresponds to the Debye relaxor, the QELS full width at half maximum (FWHM or Γ) is related to relaxation time (τ) as $\Gamma = 1/2\pi\tau$. In our case the relaxation time was of the order of 10^{-13} s. The following relation was used to describe the QELS:

$$S(\omega) = \chi''[n(\omega) + 1] \tag{8}$$

where $\chi_{QE}(\omega) = \chi_0(T)(1 - i\omega/\Gamma)^{-1}$ and $n(\omega)$ is the Bose-Einstein factor. Calculations using the least-squares method allowed us to find the temperature dependence of FWHM and susceptibility. An example of fitting of the low-frequency region of the experimental spectrum is given in Fig. 15(a). Figures 15(b) and 15(c) also shows temperature dependences of susceptibility and QELS contour width derived from the experiments in the $\mathbf{q}_{ph} \| c$ geometry. It can be seen that susceptibility exhibits a weak maximum in the vicinity of 160 K, a pronounced anomaly at 185 K, and a jump in the vicinity of 260 K [Fig. 15(b)[. The QELS width is temperature independent at $T < 225$ K and then begins to decrease [Fig. 15(c)]. A further increase in temperature gives rise to an anomaly at the temperature dependence of FWHM in the vicinity of 260 K. The behavior of susceptibility agrees well with those of permittivity and conductivity (compare Figs. 15 and 7). Therefore, it can be supposed that the behaviors of dielectric properties and quasielastic light scattering have the same mechanism; i.e., the QELS behavior is governed by evolution of localized charge carriers and formation of the layered superstructure. In all probability, in our case QELS is due to scattering from fluctuations of charge and spin densities and lattice states. Above 260 K the localized carrier concentration falls in a step and percolation conductivity increases (Fig. 7). Simultaneously, susceptibility abruptly grows and QELS FWHM decreases [Figs. 15(b) and 15(c)]. This does not contradict the idea (inferred in analysis of dielectric properties) of a phase transition at $T \approx 262$ K, at which a dynamic homogeneous layered superstructure with a balance between carrier attraction and repulsion forces is formed. As temperature further grows, percolation conductivity begins to prevail. It is likely that the quasielastic scattering mechanism changes in this temperature interval, and the contribution of electron Raman scattering typical of semiconductors becomes dominating.[32]

Thus, the results obtained in Raman light-scattering studies of ECMO are in line with the suggested model of charge-ordering-induced ferroelectricity and layered superstructure arising in the crystal due to charge self-organization above 185 K.

VI. CONCLUSION

Single crystals of diluted multiferroics–semiconductors ECMO that exhibit a giant permittivity ($\varepsilon' \sim 10^4$) above 185 K have been synthesized and studied. Complex investigations of x-ray diffraction, heat capacity, dielectric and magnetic properties, conductivity, and Raman light-scattering spectra have been carried out by both contact and contactless techniques. The experimental data obtained in our investigations can be adequately explained if we assume that the as-grown quasi-2D layers that contain doping impurities, charge carriers (electrons), and manganese ions of variable valence Mn^{3+}-Mn^{4+} are formed in ECMO normal to the c axis (1D superlattices). At low temperatures, the superlattices are electrically neutral and occupy a small volume of the crystal. The major crystal volume is occupied by the dielectric matrix of the initial EMO crystal. At $T = 5$ K in magnetic filed $H \| C$ the dHvA oscillations were observed that gives evidence for the existing superlattices. As temperature grows and, hence, the probability of thermally activated charge carrier hops from the layers increases, a layered superstructure consisting of charged layers alternating with dielectric interlayers of the initial crystal is formed. This is a dynamic state with a periodical charge distribution accompanied by lattice distortions. It can be classified as the ferroelectricity due to charge ordering leading to a giant permittivity. The ferroelectricity state arises due to a percolation phase transition at $T \approx 185$ K and exists up to 325 K. The crystal electroneutrality in this temperature interval is provided by the equality between the number of excess doping electrons and difference between the Mn^{3+} and Mn^{4+} concentrations. Double exchange between Mn^{3+} and Mn^{4+} ions that gives rise to a ferromagnetic orientation of spins of these ions plays an important role in ECMO at all temperatures. Together with the Jahn-Teller and Coulomb interactions, it forms barriers at the superstructure barrier boundaries. The presence of the layered superstructure has been confirmed in x-ray diffraction

studies of ECMO. The specific features of the Raman-scattering spectra are adequately explained by the model of ferroelectricity due to charge ordering and phase transitions in these crystals we suggest. Thus, it has been found that ECMO is indeed a multiferroic semiconductor with high enough temperatures of magnetic and ferroelectric orderings (above 185 K, including room temperature). A strong coupling between magnetic and polar states in these crystals at room temperature is achieved due to the participation of charge carriers in formation of both the magnetic and ferroelectric long-range orders.

ACKNOWLEDGMENTS

The authors would like to thank N. V. Zaitzeva for x-ray phase analysis of the samples. The work was supported by the Russian Foundation for Basic Research (Grant No. 08-02-00077) and Presidium of RAS (Programme No. 03).

*sanina@mail.ioffe.ru

[1] Y. Noda, H. Kimura, M. Fukunaga, S. Kobayashi, I. Kagomiya, and K. Kohn, J. Phys.: Condens. Matter **20**, 434206 (2008).
[2] P. G. Radaelli and L. C. Chapon, J. Phys.: Condens. Matter **20**, 434213 (2008).
[3] A. B. Harris, M. Kenzelmann, A. Aharony, and O. Entin-Wohlman, Phys. Rev. B **78**, 014407 (2008).
[4] A. M. Kadomtseva, S. S. Krotov, Yu. F. Popov, and G. P. Vorob'ev, J. Low Temp. Phys. **32**, 709 (2006).
[5] L. P. Gor'kov, Phys. Usp. **41**, 589 (1998).
[6] M. Yu. Kagan and K. I. Kugel, Phys. Usp. **44**, 553 (2001).
[7] J. van den Brink and D. I. Khomskii, J. Phys.: Condens. Matter **20**, 434217 (2008).
[8] E. I. Golovenchits and V. A. Sanina, JETP Lett. **81**, 509 (2005).
[9] E. I. Golovenchits and V. A. Sanina, JETP Lett. **84**, 190 (2006).
[10] V. A. Sanina, E. I. Golovenchits, and V. G. Zalesskii, Phys. Solid State **50**, 913 (2008).
[11] V. A. Sanina, E. I. Golovenchits, and V. G. Zalesskii, Phys. Solid State **50**, 922 (2008).
[12] V. A. Sanina, L. M. Sapozhnikova, E. I. Golovenchits, and N. V. Morozov, Sov. Phys. Solid State **30**, 1736 (1988).
[13] R. D. Shannon, Acta Crystallogr., Sect. A: Cryst. Phys., Diffr., Theor. Gen. Crystallogr. **32**, 751 (1976).
[14] Z. H. Sun, B. L. Cheng, S. Dai, K. J. Jin, Y. L. Zhou, Y. B. Lu, Z. H. Chen, and G. Z. Yang, J. Appl. Phys. **99**, 084105 (2006).
[15] E. I. Golovenchits, N. V. Morozov, V. A. Sanina, and L. M. Sapozhnikova, Sov. Phys. Solid State **34**, 56 (1992).
[16] V. Polyakov, V. Plakhty, M. Bonnet, P. Burlet, L.-P. Regnault, S. Gavrilov, I. Zobkalo, and O. Smirnov, Physica B **297**, 208 (2001).
[17] E. I. Golovenchits, V. A. Sanina, and A. V. Babinskii, Sov. Phys. JETP **85**, 156 (1997).
[18] H. Nakamura, M. Ishikawa, K. Kohn, and M. Ishikawa, J. Phys. IV France, C1, **7**, 365 (1997).
[19] C. R. dela Cruz, F. Yen, B. Lorenz, M. M. Gospodinov, C. W. Chu, W. Ratcliff, J. W. Lynn, S. Park, and S.-W. Cheong, Phys. Rev. B **73**, 100406(R) (2006).
[20] H. D. Zhou, J. A. Janik, B. W. Vogt, Y. J. Jo, L. Balicas, M. J. Case, C. R. Wiebe, J. C. Denyszyn, J. B. Goodenough, and J. G. Cheng, Phys. Rev. B **74**, 094426 (2006).
[21] D. Shoenberg, *Magnetic Oscillations in Metals* (Cambridge University Press, New York, 1984).
[22] A. R. Long, Adv. Phys. **31**, 553 (1982).
[23] *Semiconductor Superlattices. Growth and Electronic Properties*, edited by H. T. Granhm (World Scientific, Singapore, 1995).
[24] A. R. von Hippel, *Dielectrics and Waves* (Wiley, Chapman & Hall, New York, London, 1954).
[25] D. O'Neill, R. M. Bowman, and J. M. Gregg, Appl. Phys. Lett. **77**, 1520 (2000).
[26] B. Mihailova, M. M. Gospodinov, B. Guttler, F. Yen, A. P. Litvinchuk, and M. N. Iliev, Phys. Rev. B **71**, 172301 (2005).
[27] A. F. García-Flores, E. Granado, H. Martinho, R. R. Urbano, C. Rettori, E. I. Golovenchits, V. A. Sanina, S. B. Oseroff, S. Park, and S.-W. Cheong, Phys. Rev. B **73**, 104411 (2006).
[28] J. Cao, L. I. Vergara, J. L. Musfeldt, A. P. Litvinchuk, Y. J. Wang, S. Park, and S.-W. Cheong, Phys. Rev. B **78**, 064307 (2008).
[29] K. Yamamoto, T. Kimura, T. Ishikawa, T. Katsufuji, and Y. Tokura, Phys. Rev. B **61**, 14706 (2000).
[30] I. G. Siny, S. G. Lushnikov, R. S. Katiyar, and E. A. Rogacheva, Phys. Rev. B **56**, 7962 (1997); I. G. Siny, S. G. Lushnikov, R. S. Katiyar, and V. H. Schmidt, Ferroelectrics **226**, 191 (1999).
[31] *Light Scattering Near Phase Transitions*, edited by H. Z. Cummins and A. P. Levanyuk (North-Holland, Amsterdam, 1983).
[32] B. H. Bairamov, I. P. Ipatova, and V. A. Voitenko, Phys. Rep. **229**, 221 (1993).
[33] S. N. Gvasaliya, B. Roessli, R. A. Cowley, P. Huber, and S. G. Lushnikov, J. Phys.: Condens. Matter **17**, 4343 (2005).